Original Articles

Accuracy of Least Squares Designed Spatial FIR Filters for Segmentation of Images of Fluorescence Stained Cell Nuclei

Jeffrey H. Price, Edward A. Hunter, and David A. Gough

Departments of Bioengineering (J.H.P., D.A.G.), and Electrical and Computer Engineering (E.A.H.), Institute for Biomedical Engineering, University of California, San Diego, La Jolla, California

A method for accurate, real-time image segmentation is needed for the development of a fully automated image cytometer that combines the speed and ease-of-use of flow cytometry with the detailed morphometry of imaging. Object intensity variation and inherent optical blur make real-time segmentation challenging. The best spatial finite impulse response (FIR) filter, implemented as a convolution, was tested for sharpening edges and creating the required contrast. The filter and threshold segmentation steps were treated as a two-category linear classifier. Best 3 × 3 through 25 × 25 filters were designed utilizing the perceptron criterion and nonlinear least squares, and tested on ten montage images of a combined 1,070 manually segmented DAPI stained cell nuclei. The resulting image contrast, or class separation, led to simple automatic thresholding via the histogram intermodal minimum. Image segmentation accuracy began to plateau at 7 × 7 filters and did not increase above 15 × 15. Little loss in accuracy occurred with application to the images not used for design. This segmentation method provides a systematic, fast and accurate means of creating binary object maps useful for subsequent measurement, processing and cell classification.

© 1996 Wiley-Liss, Inc.

Key terms: Contrast enhancement, automated threshold prediction, object recognition, edge detection, scanning image cytometry, morphometry.

Accurate, real-time image segmentation is needed for fully automated image cytometry. Cell discrimination and measurement must be preceded by computerized segmentation, or division of the image pixels into object and background in order to achieve operator-independent automation. The inherent object-background contrast of fluorescence images suggests the possibility of detecting objects by simple intensity thresholding, but large variations of intensity within and between these objects makes accurate segmentation more difficult. This challenge is further increased by the need for high speed operation. Morphometry derived from the binary segmentation map will benefit many applications, especially when combined with the speed, ease-of-use and large measurement sample sizes of the flow cytometer. To approach the 1–10 kHz cell measurement rate of the flow cytometer for analysis of 100,000 cells on a microscope slide, image segmentation must occur as fast as image acquisition. The achievement of real-time operation, however, is complicated both by the large two-dimensional data set and the dependency of spatial measurements on segmentation accuracy. Measurements such as perimeter, area and shape, for example, degrade more with errors in segmentation than integrated intensity. Thus, although little attention has been previously given to measurement of segmentation accuracy and standards for comparison, the design of systematic techniques is an important consideration in the development of scanning cytometry.

Fluorescence image segmentation cannot be achieved accurately by simple intensity thresholding because of

the combination of image blur and the inherent intensity differences of the objects. With 8-bit image digitization, for example, it is common for the fluorescent stained cell nuclear images to range through all available intensities. Due to inherent optical limitations, some blur is always present at the edges of these objects. This blur causes the best threshold to be dependent on the brightness. One possible approach to this problem is to adapt the threshold to match the intensity of the object. Lockett et al. (13) and Price and Gough (19) have described semi-automated and fully automated versions, respectively, of adaptive thresholding for fluorescence stained cell nuclei. Adaptive thresholding requires iterative sampling of different regions of the image in order to choose the best threshold and this is difficult to carry out in real-time. An alternative is to use a spatial FIR filter to sharpen the image prior to application of the threshold. If the FIR filter can perform the correct high contrast enhancement, the necessary convolution operation may be performed in real-time using commercially available image processing hardware. This should improve the accuracy of the resulting image segmentation, regardless of whether the subsequent threshold operation is a single, global one or an adaptive, regional one.

Many of the previously used image segmentation methods were reviewed by Fu and Mui (5) and Pal and Pal (15). For a few of the techniques reviewed, methods of measuring the accuracy of the segmentation were utilized. Levine and Nazif (10) used a two-dimensional distance measure to compare the difference between the manually-segmented and machine-segmented images, and also (11) defined parameters including region uniformity, region contrast, region pattern and line contrast as automated measures of segmentation accuracy. Lim and Lee (12) computed the probability of error between manually and automatically segmented images. Pal and Bhandari (16) used the higher order local entropy as an index to measure the quality of the output. At present, however, there is no agreed upon standard objective method for evaluation and human discrimination is considered the best judge of segmentation quality (15). Most of the image segmentation techniques in the previous reviews are computationally intensive and difficult or impossible to implement economically in real-time, and for this reason are not evaluated here.

Neighborhood operators other than FIR filters have been used for machine vision applications such as integrated circuit (IC) inspection. Dom et al. (2) discussed the use of these in supervised image segmentation methods. Instead of using all of the parameters in the neighborhood, as with an FIR filter, these IC implementations first transform the neighborhood into a reduced set of features (e.g., mean, minimum, maximum, median, gradient magnitude, and Laplacian), then combine them linearly to produce an output that is thresholded for image segmentation. The number and complexity of these operations can complicate real-time implementation. These methods are usually applied to objects with predictable geometric shapes and uniformly high contrast rather than to amorphous biolog-

ical objects of differing intensities that result in nonstationary images. Although the examples of nonlinear neighborhood operators above (minimum, maximum, and median) are important in some applications, they do not completely characterize the neighborhood. In particular, information regarding the relative structural distributions of intensities may be lost. The inhomogeneity of biological objects suggests this information to be particularly important for class separation.

In order to obtain high-quality measurements of clinically useful morphometric parameters such as area, perimeter, pattern, and shape, the edges of the objects should first be located accurately. If the goal was only to perform object recognition and record the number and locations of objects, as is common with many other machine vision applications, the segmentation accuracy would not be of crucial importance. For these images, the task of *recognition* of the image objects, or cell nuclei, is greatly simplified by the specificity of the fluorescence staining. All bright objects can be assumed, for the purposes of the image segmentation step, to be cell nuclei. The goal is then to classify accurately the pixels of all bright objects, with the assumption that subsequent processing will be applied for further classification (e.g., to identify overlapping cells, the cell cycle phase or cell type). With the segmentation step completed and data about each object collected, higher level object classification steps can be carried out quickly on the measured data rather than on much larger images. This narrow definition of segmentation simplifies implementation for real-time operation, and error analysis for filter design. These considerations led the efforts reported here to be directed at measuring and improving the accuracy at the level of the image pixels.

The segmentation method was chosen to combine the linear transform of low-order spatial FIR filters with cost-effective implementation of the convolution operation in real-time on commercially available hardware. With the underlying object recognition task substantially completed by the specificity of the fluorescent dye, the FIR model contains the sharpening capability necessary for completing the task of accurate segmentation. The hypothesis that the "best" FIR filter would increase the sharpness and object-background contrast and result in simplification of the subsequent threshold step, was the basis of the technique chosen for filter design. For image G, segment S, and spatial FIR filter K, the segmentation procedure is

$$F = K*G$$
$$S = \begin{matrix} C_0, F < T \\ C_1, F \geq T \end{matrix} \qquad (1)$$

where * is the convolution operator, F is the filtered image, T is the threshold, and C_0 and C_1 represent the two classes of the segmented images. This function is a two-category linear classifier implemented as a spatial FIR filter.

Given the input image G and an ideal segmented image I_s, it is possible to solve for the FIR filter that best maps

G to I_s. The error criteria reviewed above utilized different similarity measures of the classes *after* thresholding and did not account for the fact that the threshold choice itself is a source of error. Instead of focusing on classification error after thresholding as a means of filter design, the strategy used here was to minimize the pixel-by-pixel error from an arbitrary object-background contrast in an effort to achieve error insensitive to the subsequent threshold. Therefore, although the proportion of correctly classified pixels was later utilized to measure the combination of the success of filter design and threshold choice, the error criterion chosen for design of the filters was fundamentally different. The perceptron criterion, widely used in classification schemes, provides this error measure. The use of a margin with the perceptron criterion incorporates the importance of achieving a minimum contrast between the background and object classes in order to reduce the errors expected in subsequent thresholding. These methods are explained by Duda and Hart (3). The criterion can be written

$$E = \sum \begin{cases} (I_s - F)^2; & A < F < B \\ 0; & \text{otherwise} \end{cases} \qquad (2)$$

where error E is nonzero only when the filter has not achieved the contrast defined by [A, B]. Minimization of E yields a filter K that creates the best contrast for subsequent thresholding within [A, B], where "best" is defined by the criterion function and the ideal image used as a standard. In these equations, S and I_s represent whole objects rather than edges in order to limit the reconnection problems associated with strictly edge-finding routines. This choice may also decrease the sensitivity of the method to errors in the ideal image used as the standard. A version of Equations 1 and 2 was also presented by Hunter et al. (8).

The following describes a series of experiments designed to measure the contrast enhancement, resulting threshold insensitivity, and segmentation accuracy of these methods on images of fluorescence stained cell nuclei.

MATERIALS AND METHODS
Cells and Specimen Preparation

NIH 3T3 cells were cultured on washed, autoclaved #1.5 coverslips. The cells were maintained in Eagle's minimal essential medium with Earle's salts, supplemented with 10% fetal bovine serum, 100 µg/ml gentamicin, and 0.26 mg/ml L-glutamine (final concentrations), in a humidified 5% CO_2 incubator at 37°C. After 1 day of cell growth, the coverslips were rinsed in phosphate buffered saline (PBS), fixed for 10 min in 4% paraformaldehyde in 60% PBS, and stained for 1 h. The stain solution consisted of 75 ng/ml 4',6-diamidino-2-phenylindole dihydrochloride (DAPI, Molecular Probes, Eugene, OR), 10 mM Tris, 10 mM EDTA, 100 mM NaCl, and 2% 2-mercaptoethanol, as described by Hamada and Fujita (7), who found it to exhibit excellent antiphotobleaching properties. After staining, a few drops of DAPI solution were placed on a glass slide, the coverslips were laid down, excess solution was removed, and the coverslips were sealed to the slide with nail polish.

Microscopy and Image Acquisition

The cells were imaged on a Nikon Optiphot through a CF Fluor DL ×20, 0.75 NA objective. This fluorite objective provides high UV transmission. The epifluorescence filter cube had a 365 nm ± 10 nm (50% of peak) bandpass excitation filter, a 400 nm dichroic mirror and no barrier filter. The images were acquired with a Dage VE 1000 RS-170 CCD camera and digitized by an Imaging Technology Inc. (Woburn, MA) Series 151 image processor. The area of the specimen projected onto a single camera element was 0.620 × 0.514 µm². The image processor was controlled by an Intel-based 486 host computer. The epifluorescence source was a 100 W Hg vapor arc lamp. Camera level was adjusted until all background intensities were digitized > 0, and gain was adjusted until the brightest fluorescence intensities were digitized < 255. Price and Gough (20) provided additional description of the use of this equipment in scanning and autofocus.

Training and Image Processing

Ten test montage images were created by combining image areas containing unusually bright, dim, or high contrast nuclei from many different microscope fields. These nuclear images were chosen because wide intensity differences are the most difficult to segment accurately. One or more different microscope slides were used for each of these ten resulting composite images in order to test whether or not normal variations in specimen preparation, light intensity and camera settings that vary from image to image would alter performance. The images were collected in 2 sets of five. The second set was collected with the constraints of a minimum average nuclear intensity of 20 and a minimum internuclear distance of 30 pixels. The minimum intensity was chosen after preliminary results from the first set indicated that extremely low intensity nuclei were more difficult to enhance. The minimum internuclear distance was set to greater than the maximum FIR filter size after noting that the classification ratios did not seem to improve above a filter size of 15 × 15. The concern was that the close packing of the nuclear image objects, causing neighborhoods of larger filters to contain more than one nucleus, might compromise performance. Images 1 and 2 were collected at much higher gain than the others due to initially unrecognized low lamp intensity which gave these images a noticeably lower signal-to-noise ratio.

Corresponding interactively defined ideal images were created from a sharpened version (filter defined below) of the montage images. The edges were drawn under cursor control and comparison was made with the unsharpened original montage images to ensure against inappropriate edge breaks. After high-intensity edges were drawn in, the ideal images were created by intensity thresholding, the thresholded images were run-length encoded, the run-lengths were sorted into data structures of

connected objects as detailed by Price (18), and holes were filled automatically as described by Jain (9).

The perceptron criterion implemented with a margin as in equation (2) was chosen to create an arbitrary amount of contrast, or class separation. This class separation was expected to improve segmentation accuracy and automatic threshold prediction in the presence of noise and other unpredictable and nonlinear sources of degradation (e.g., blur caused by higher-order optical aberrations). The values of A and B in Equation 2 were set to 0 and 255, respectively, in order to match the digitization range and create high enough contrast to simplify threshold prediction, and yet not overwhelm the limited integer range of real-time image processing hardware. The choice of contrast range is also important for threshold selection methods that utilize intensity histograms. Even in integer hardware the intermediate result of the filter is represented by more bits (16–32) than the histogram intensities (8–10 bits). Therefore, filtered pixel values must scaled to the histogram, and contrast should be large enough to retain the histogram detail required for threshold prediction.

Hole filling and size thresholding on run-length encoded representations of the image objects were used after intensity thresholding to improve the segmented images. These operations were not performed prior to accuracy measurements in order to simplify evaluation of the performance of the error criterion of equation (2). With the hardware run-length encoding of the Series 151 image processor, these operations can take place in real-time due to the advantage of the run-length data compression. The number of operations required for sorting the run-lengths is proportional to the sum of the vertical lengths of the objects and their branches. Geometric measures such as size can be computed during sorting and objects below a given size eliminated from the data structure. With similarly sorted run-lengths of the background, the holes are defined as those background objects that are not connected to the edges of the image as described by Russ (22,23), or by divergence and subsequent convergence of the run lengths during sorting as described by Jain (9). The erosion/dilation techniques of mathematical morphology were considered for filling holes and removing noise, but they have the disadvantages of computational complexity proportional to the area and alteration of the edge characteristics of the objects.

Computer Software and Hardware

The input and ideal images were transferred to Silicon Graphics Inc. (SGI) workstations for least squares design of the FIR filters. The software was modified from the Press, et al. implementation (17) of the Levenberg-Marquardt method of nonlinear least squares error minimization. The most important modification was the addition of a conditional check for avoiding calculation of the covariance matrix when the filter achieved zero error as described in Equation 2; this resulted in a speed increase of as much as four fold for filter design. Covariance matrix calculation is the major computational bottleneck in

this least squares technique. Forcing kernel symmetry would be another method of reducing computation time, but by limiting the number of parameters in the model, this would be expected to reduce segmentation performance, especially for smaller kernel sizes. In addition, with rectangular CCD pixels resulting in different vertical and horizontal sampling and other possibly more unpredictable electronic sources of distortion, caution would be prudent in forcing symmetry. FIR kernels of sizes 3 × 3 to 25 × 25 were designed on each of the ten images. Odd filters with equal horizontal and vertical dimensions were chosen for programming simplicity. The 3 × 3 filters, with 9 kernel elements (a 9 × 9 inversion matrix) each initialized to 1/9, took less than a minute and required 12 iterations to achieve a change in the error of equation (2) of < 0.01 (SGI 200 MHz R4400 processor). The 25 × 25 filters, with 625 elements (a 625 × 625 inversion matrix) took about 6 hours and 4 iterations to achieve the same change in error using the previous 23 × 23 filter, padded with zeros to 25 × 25, for initialization.

Laplacian and sharpen convolution kernels were used for comparison with perceptron trained filters and for creation of the edge maps from binary images, respectively. There are many different implementations of these operations represented in the literature. For this report,

$$\begin{bmatrix} -1 & -1 & -1 \\ -1 & 8 & -1 \\ -1 & -1 & -1 \end{bmatrix} \quad \begin{bmatrix} -1 & -1 & -1 \\ -1 & 9 & -1 \\ -1 & -1 & -1 \end{bmatrix}$$

are the related Laplacian and sharpen kernels, respectively. Many filters could have been chosen for comparison along with the sharpen filter, but the goal was to explore a method for designing the best FIR filters. The sharpen filter was chosen to emphasize the point that the choice of the filter is nontrivial. That is, if any sharpen filter worked well there wouldn't be much use in expending the effort to design the best one.

Segmentation Error Analysis

The error criterion, Equation 2, used for design of the filters was chosen with the goal of expanding the separation between object and background classes in order to simplify thresholding. This error criterion does not, however, describe the error in segmentation that necessarily includes thresholding. To describe the combined segmentation accuracy the classification ratio was defined as 1 − (misclassified pixels)/(object pixels), where the number of object pixels is defined by the manually segmented image. This is a conservative measure that penalizes for both background and object pixel classification errors, but is scaled only by the number of object pixels in the image. Classification ratios were calculated for each of the 12 filters applied to each of the ten images for a total of 1,200 data points.

RESULTS
Test Images and Example Filters

Table 1 is a compilation of summary data characterizing the ten montage images, which contained a total of

Table 1
Summary Data of Training Images of Fluorescence Stained Cell Nuclei

Image	Nuclei	Mean intensity[a]	Contrast [CV, %][a]	Area[b]
1	103	68 ± 35 [18, 163]	32 ± 9 [19, 57]	765 ± 328 [190, 1747]
2	106	73 ± 38 [18, 157]	34 ± 8 [21, 58]	894 ± 487 [294, 2937]
3	104	76 ± 43 [16, 161]	40 ± 9 [26, 62]	908 ± 375 [276, 2753]
4	173	74 ± 40 [14, 159]	37 ± 8 [24, 63]	571 ± 330 [147, 1850]
5	162	71 ± 40 [13, 177]	36 ± 8 [20, 68]	635 ± 459 [172, 4186]
6	84	76 ± 45 [20, 193]	32 ± 5 [18, 50]	634 ± 403 [79, 2106]
7	87	91 ± 53 [23, 187]	34 ± 6 [22, 52]	549 ± 284 [132, 1450]
8	76	77 ± 41 [23, 148]	35 ± 5 [26, 52]	652 ± 361 [192, 1645]
9	89	83 ± 41 [23, 180]	33 ± 4 [24, 47]	469 ± 317 [121, 1546]
10	86	79 ± 42 [21, 146]	37 ± 7 [27, 60]	499 ± 321 [158, 1405]

[a]Mean ± S.D. [Minimum, Maximum] in digital intensity.
[b]Mean ± S.D. [Minimum, Maximum] in pixels (1 pixel = 0.319 μm^2).

1,070 nuclei. The intensity, contrast (intensity coefficient of variation, %), and area are included as descriptions of the variability of images of cell nuclei. The ideal images were used as masks for the intensity and contrast measurements, and areas were measured directly from the ideal objects. The differences among images are useful in evaluating potential problems that might arise from designing a filter on one image and applying it to another.

Examples of filters designed using least squares are shown in Figure 1. Since 120 filters were designed for the experiments reported here, and the largest of these (25 × 25) consists of 625 elements, it is impractical to include even a representative set of all sizes. The following characteristics of the 3 × 3, 5 × 5, 7 × 7, 15 × 15 and 25 × 25 kernels shown in Figure 1, though, are common to the entire set. There is a pattern of a positive number in the center, or target location, and some negative numbers in the outer positions, indicative of highpass, or sharpen characteristics. The mixture of negative and positive numbers in the outer positions and the incomplete radial symmetry, however, suggest a more complicated mixture of spatial frequency enhancement and phase characteristics than is present in a simple highpass filter. This follows from the generality of the error minimization technique used for design. The design method does not constrain the enhancement characteristics, or phase and symmetry properties of the FIR filters in any way. Since these filters are the best possible under the design criteria, it is reasonable to assume that imposing symmetry or other constraints would decrease the segmentation accuracy for a given filter size.

Contrast Enhancement

The contrast enhancement resulting from the application of some of the least squares designed filters is exhibited in the intensity mesh plots of the fluorescence stained cell nuclei in Figure 2. The montage of three images shown in Figure 2a demonstrates the finite slopes at the edges of a bright mitotic nucleus, a dim resting nucleus and a high contrast nucleus. It is easy to see from these edge slopes that the best thresholds vary from nucleus to nucleus and would be different even along the

edge of the same nucleus. For comparison, the maximum slopes possible in the digitized image are visible in the 3D plots of the hand-segmented ideal images in Figure 2h. The problem caused by the internal structure of the images is shown in Figure 2b, the result of a conventional sharpen filter. Although the simple sharpen filter works well on the bright mitotic nucleus, the internal structure of the other two nuclei creates numerous spurious edges that connect with the true outer edges. These broken edges require more computationally intensive algorithms for reconnection and add uncertainty regarding the location of the intervening true edges.

Solving for a best filter to enhance contrast becomes a simple linear least squares problem if an exact fit is required between the original and ideal images. The exact fit was achieved by excluding the conditional portion of Equation 2. Examples of using two such exact fit filters, a 3 × 3 and a 15 × 15 are shown in Figure 2c,d. These two examples show that it is very difficult for exact fit filters to provide the right combination of contrast enhancement and sharpening. Note in particular that the sharpness of the bright mitotic nucleus with the larger 15 × 15 filter was actually less than with the smaller 3 × 3 filter.

Examples of the results of perceptron-trained filters, designed using Equation 2, are shown in Figure 2e–g. The improved contrast and edge sharpness are immediately obvious, and the improvement is noticeable on all three nuclei. The sharpness of the bright mitotic nucleus improved with increasing filter size, unlike with the exact fit filters. Improvements in the dim and high contrast nuclei with increasing filter size were more subtle, but it is clear that the contrast enhancement on the dimmer nuclei was not compromised by the increase in sharpness on the bright one.

The classifier fit filters achieved this increase in contrast by scaling and sharpening the images. With a constant image of equal pixels, an FIR filter only multiplies the image. This scale is the sum of the kernel parameters. The mean scale of all classifier fit filters was 8.3. Thus, constant regions of the images were multiplied by 8.3.

In a separate experiment, the effect of the scale was tested by changing the filter operation in Equation 1 to
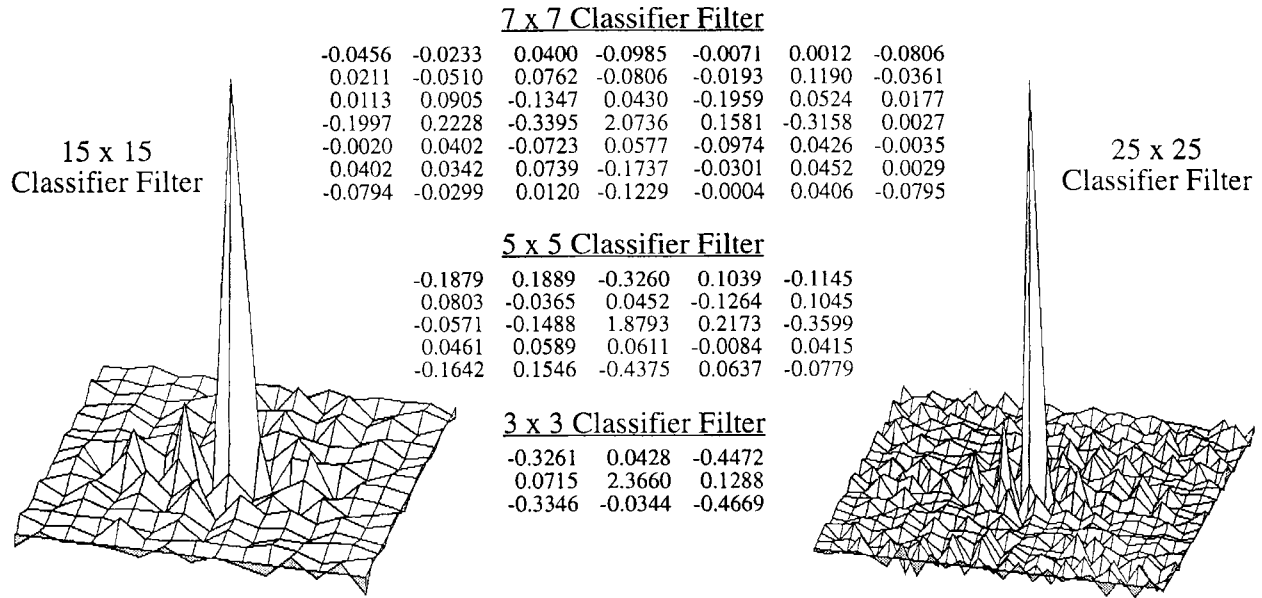
7 x 7 Classifier Filter

-0.0456	-0.0233	0.0400	-0.0985	-0.0071	0.0012	-0.0806
0.0211	-0.0510	0.0762	-0.0806	-0.0193	0.1190	-0.0361
0.0113	0.0905	-0.1347	0.0430	-0.1959	0.0524	0.0177
-0.1997	0.2228	-0.3395	2.0736	0.1581	-0.3158	0.0027
-0.0020	0.0402	-0.0723	0.0577	-0.0974	0.0426	-0.0035
0.0402	0.0342	0.0739	-0.1737	-0.0301	0.0452	0.0029
-0.0794	-0.0299	0.0120	-0.1229	-0.0004	0.0406	-0.0795

15 x 15 Classifier Filter

25 x 25 Classifier Filter

5 x 5 Classifier Filter

-0.1879	0.1889	-0.3260	0.1039	-0.1145
0.0803	-0.0365	0.0452	-0.1264	0.1045
-0.0571	-0.1488	1.8793	0.2173	-0.3599
0.0461	0.0589	0.0611	-0.0084	0.0415
-0.1642	0.1546	-0.4375	0.0637	-0.0779

3 x 3 Classifier Filter

-0.3261	0.0428	-0.4472
0.0715	2.3660	0.1288
-0.3346	-0.0344	-0.4669

FIG. 1. Example least squares designed FIR filters of sizes 3 × 3, 5 × 5, 7 × 7, 15 × 15, and 25 × 25, trained on Image 4, and each scaled to sums of 1.0.

$$F' = \frac{R}{\sum_{ij} k_{ij}} (K^\bullet G), \tag{3}$$

where k_{ij} are the parameters of the kernel and R is the imposed scale. Using this filter function in the error criterion of Equation 2 allowed testing of different scales. Scales lower than 8.3 gave insufficient contrast for the margin of [0, 255] and compromised segmentation accuracy. Above scales of 8.3, the accuracy did not improve further. Thus, both the multiplicative scale factor and the sharpening are required for the filters to create arbitrary contrast.

Threshold Sensitivity

The goal of the filter design was to produce an image that could be thresholded at a wide range of intensity values with high segmentation accuracy. This high level of accuracy is important because of its expected effect on the accuracy of important morphometric parameters. For simplicity and speed it would be best if the segmentation were accurate over a wide range of thresholds for all objects. This is most difficult for those objects with the largest difference in intensity. Figure 3 shows threshold sensitivity plots for a very bright nucleus and a very dim nucleus, with average digital intensities of 150 and 17 respectively. The threshold sensitivities are shown for no filter and a 3 × 3 sharpen filter in Figure 3a; and 15 × 15 exact fit and 15 × 15 perceptron-trained filters in Figure 3b.

The threshold sensitivity curves of Figure 3a show the large difference between the best thresholds of the dim and bright nuclei with no filter operation. The intersection of these two curves, shown by the arrow at an intensity of 93 in Figure 3a is the approximate best single threshold, at a classification ratio of 0.72, for both nuclei. The sharpen filter, for which results are also shown in Figure 3a, breaks the dim nucleus so much that even the best threshold correctly classifies only about half of the object pixels. Thus, even though the threshold sensitivity curves are not as separated as with no filter, the performance is very poor with the simple sharpen filter.

Figure 3b shows threshold sensitivity curves for 15 × 15 exact and perceptron-trained filters on the same dim and bright nuclei. The best combined threshold of 113 after application of the exact fit filter occurred at a classification ratio of 0.28, which is even worse than for the sharpen filter shown in Figure 3a. The perceptron-trained 15 × 15 filter in Figure 3a, however, shows a best combined threshold of 69 with a classification ratio of 0.91, far better than with the other examples.

Figure 3 demonstrates the thresholding problems with objects of markedly different intensity and indicates that a considerable advantage can be expected for the perceptron-trained filters. The two nuclear images chosen for Figure 3 are near the intensity extremes for nuclei compiled for these experiments. Thus it also should be expected that the combined performance will be better than for these extremes.

Performance Dependence on Filter Size

The size of the FIR filter required for accurate segmentation is important because of the requirement for real-time operation. With large kernels, the convolution operation is more efficiently performed using the fast Fourier transform (4). Hardware implementations of

a) Original Images

b) Sharpen (3 x 3)

c) Exact Fit (3 x 3)

d) Exact Fit (15 x 15)

e) Classifier Fit (3 x 3)

f) Classifier Fit (7 x 7)

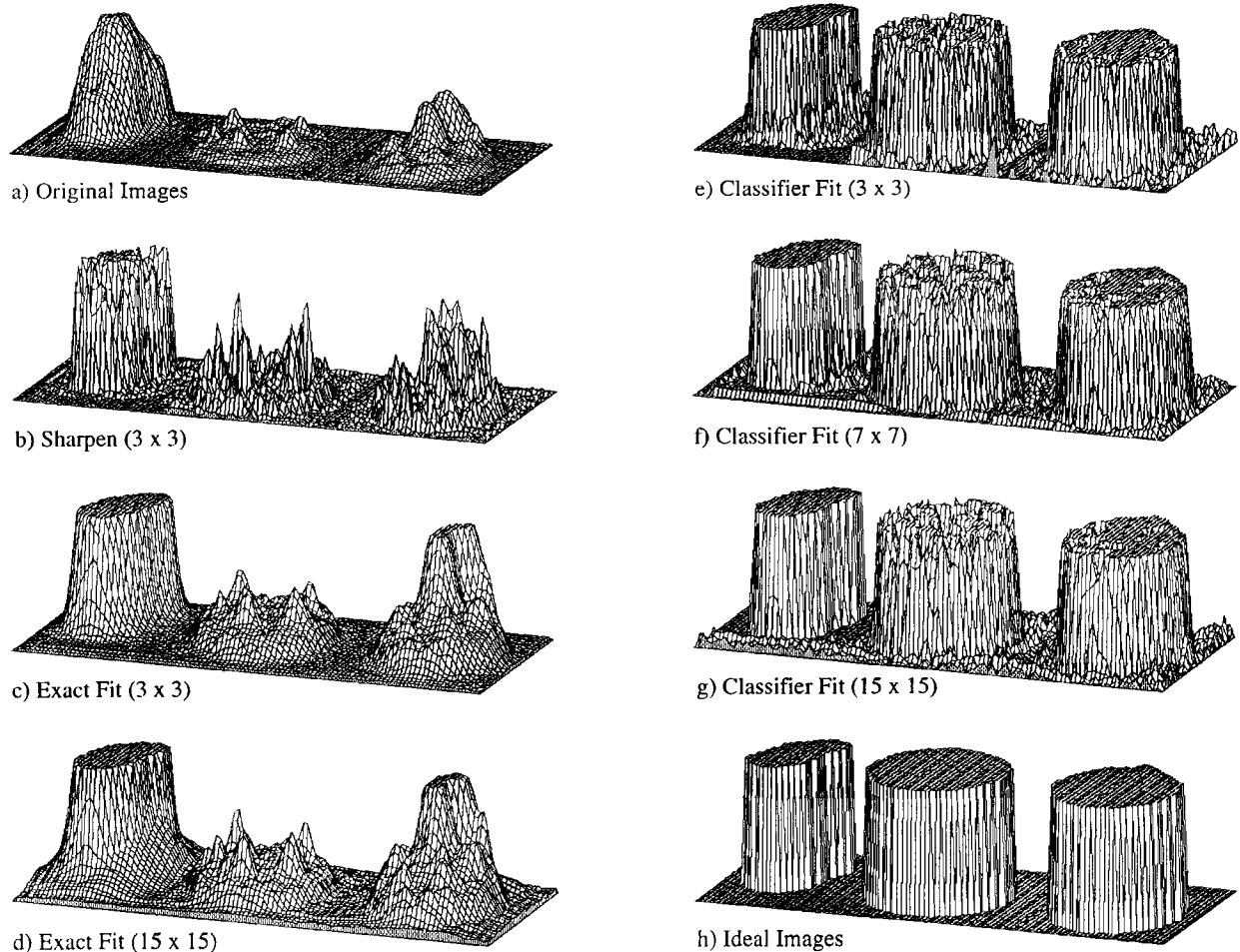g) Classifier Fit (15 x 15)

h) Ideal Images

Fig. 2. Mesh plots of the intensity of bright (mitotic), dim (resting) and high contrast nuclei (64, 97, and 164 in Fig. 6; left to right in each). a: Original images. b: Result of a sharpen filter (3 × 3 with ·1s and 9 target). c,d: Results of 3 × 3 and 15 × 15 linearly designed, exact fit filters. e–g: Results of 3 × 3, 7 × 7, and 15 × 15 nonlinearly designed, classifier fit filters. h: Ideal images. All plots except a) were clipped [0, 255] to magnify the threshold region.

small kernel convolutions are common up to a size of 8 × 8 and practical up to a size of about 16 × 16 in commercial systems.

The dependence of the classification ratio on filter size was compared by analysis at the best thresholds. Two regions, edge and whole object, were defined for computing the classification ratio. The edge region was defined as the two-pixel wide region that is the combination of background and object edges. The object edges were found from the Laplacian of the ideal image and the background edges were found by applying the negative of the Laplacian. The best thresholds were determined from the threshold sensitivity data on each filter.

Table 2 gives the average segmentation performances for no filter (identity), the sharpen filter and each of the perceptron-trained filter sizes. The edge-region performance of the sharpen filter was much better than with no filter, but the whole-object performance was much worse. This helps explain the poor threshold sensitivity results

for the sharpen filter in Figure 3a. The sharpen filter breaks the dim objects into many pieces, complicating accurate reconstruction. For the classifier designed filters, the classification ratio reaches a maximum quickly with < 0.5% improvement for filters larger than 7 × 7 and < 0.25% improvement for filters larger than 9 × 9. For filters larger than 17 × 17 the performance actually worsens with larger filters in some cases, although these differences are so small that the numbers may be statistically equivalent. Since it is difficult to predict the relationship between size and accuracy, and it is possible for accuracy to improve again at some larger size, the complete data set is shown. In addition, selected 35 × 35 filters were designed and tested with no further improvement exhibited. These comparisons show that while there are small advantages to filters larger than 9 × 9, there may be no advantage to using filters larger than 15 × 15. Commercially available real-time image processing hardware is thus capable of performing the necessary task.
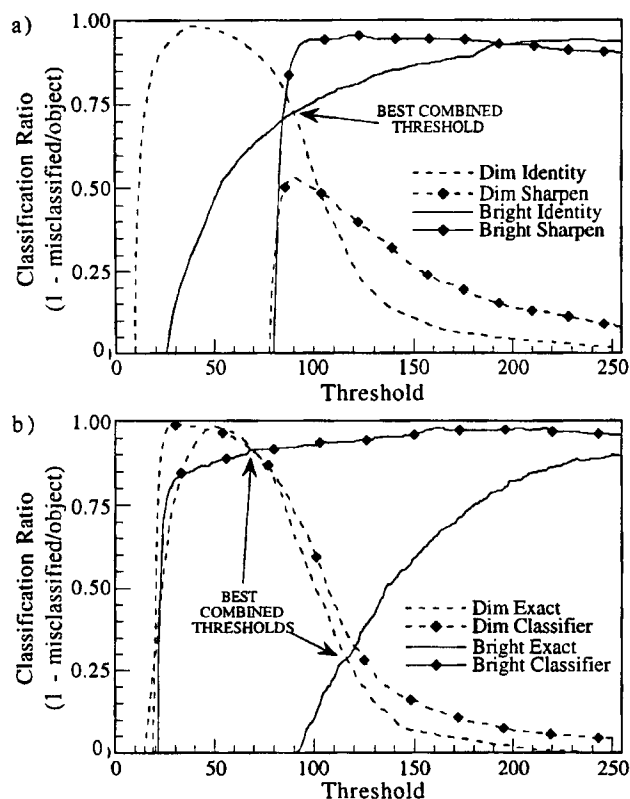
FIG. 3. Threshold sensitivity of bright and dim nuclei. a: No filter and a conventional 3 × 3 sharpen filter. b: 15 × 15 exact fit and classifier filters.

Table 2
Segmentation Accuracy vs. Filter Size

	Classification Ratio	
Filter	Object	Edge
Identity	0.88093	0.74240
Sharpen	0.76758	0.88721
3 × 3	0.91686	0.83769
5 × 5	0.93049	0.85420
7 × 7	0.93298	0.85738
9 × 9	0.93452	0.85964
11 × 11	0.93522	0.86055
13 × 13	0.93561	0.86121
15 × 15	0.93584	0.86156
17 × 17	0.93586	0.86163
19 × 19	0.93576	0.86156
21 × 21	0.93568	0.86150
23 × 23	0.93550	0.86143
25 × 25	0.93528	0.86150

Threshold Prediction

The FIR filters were designed to create separation between object and background classes in order to simplify thresholding. With increased class separation, there are two possible approaches to choosing the threshold that finalizes segmentation. These are a fixed threshold, which for [A, B] in Equation 2 set to [0, 255] would be
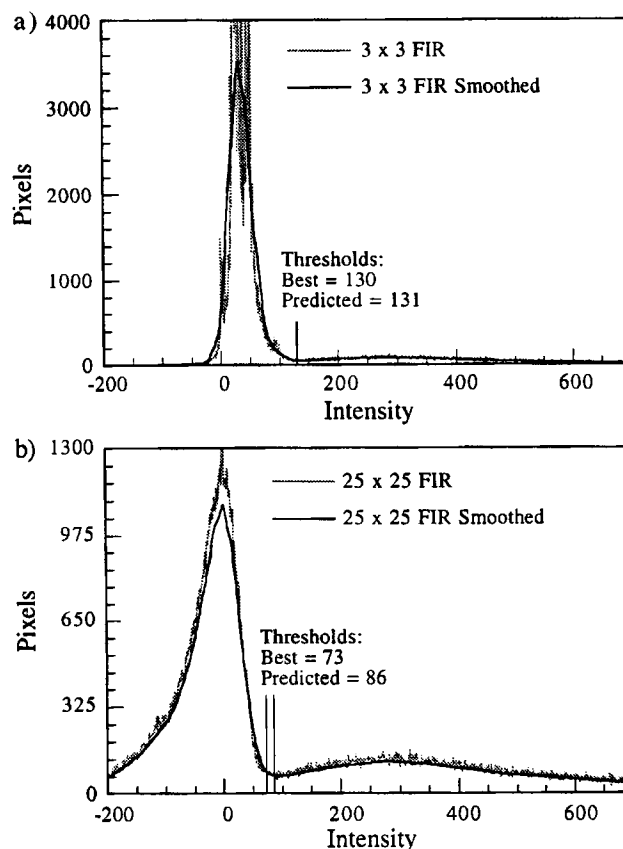

FIG. 4. Original and smoothed intensity histograms of filtered images. a: 3 × 3 designed on Image 9 and applied to Image 8. b: 25 × 25 designed on Image 6 and applied to Image 3.

expected to be near 128, and a variable threshold, which could be chosen independently from the histogram of each filtered image. With the 10-bit histogram available hardware, the variable threshold step can also be carried out in real-time.

In choosing a variable threshold prediction method, it is useful to understand the expected distribution of a filtered image. Many automatic threshold techniques assume Gaussian distributions for the background and object intensities. As the result of a linear combination of Gaussian distributed intensities, each filtered pixel is also Gaussian distributed. But the mean and S.D. of the Gaussian depend on the combination of the two underlying distributions in each neighborhood of the original image. The number of possible combinations for application of a filter with an n × n neighborhood is 2^{n^2}. Thus, the filtered image consists of a very large mixture probability density function. This explains why optimal thresholding techniques that assume mixture distributions of two Gaussians performed poorly. One reason for this is that a Gaussian is a poor approximation of the mixture distribution. This can be seen from the histograms in Figure 4. Note in particular the marked asymmetry of the background peak in Figure 4b. Optimal methods tested in-

Table 3
Thresholds: Best, Fixed, and Predicted

Filter	Best		Fixed			Predicted		
	Threshold[a]	Classification ratio[a]	Threshold	Classification ratio[a]	% error vs. best	Best predicted[a]	Classification ratio[a]	% error vs. best
Identity	15.8 ± 36.0	0.88094 ± 3.637	16	0.86314 ± 3.22	2.02	b		
Sharpen	17.9 ± 37.2	0.76725 ± 3.943	18	0.74440 ± 3.93	2.98	b		
3 × 3	142.9 ± 17.4	0.91710 ± 1.525	143	0.89712 ± 3.31	2.18	1.1 ± 7.3	0.91491 ± 1.604	0.238
5 × 5	127.4 ± 19.8	0.93090 ± 1.028	127	0.91181 ± 2.32	2.05	1.1 ± 7.1	0.92990 ± 1.041	0.107
7 × 7	124.2 ± 20.8	0.93345 ± 0.990	124	0.91467 ± 2.01	2.01	1.1 ± 7.1	0.93245 ± 1.025	0.107
9 × 9	123.2 ± 21.2	0.93502 ± 0.965	123	0.91669 ± 1.84	1.96	0.3 ± 7.9	0.93405 ± 0.988	0.104
11 × 11	121.7 ± 21.5	0.93577 ± 0.943	122	0.91770 ± 1.69	1.93	1.2 ± 7.9	0.93475 ± 0.965	0.109
13 × 13	121.6 ± 21.9	0.93615 ± 0.924	122	0.91833 ± 1.57	1.90	1.3 ± 8.1	0.93507 ± 0.956	0.115
15 × 15	120.8 ± 22.3	0.93639 ± 0.921	121	0.91866 ± 1.51	1.89	1.0 ± 7.8	0.93531 ± 0.943	0.115
17 × 17	120.7 ± 22.7	0.93642 ± 0.918	121	0.91881 ± 1.49	1.88	1.0 ± 8.3	0.93534 ± 0.939	0.115
19 × 19	120.4 ± 22.8	0.93632 ± 0.908	120	0.91855 ± 1.51	1.90	2.2 ± 8.3	0.93527 ± 0.925	0.112
21 × 21	120.4 ± 22.5	0.93624 ± 0.904	120	0.91850 ± 1.49	1.89	1.7 ± 8.4	0.93512 ± 0.904	0.120
23 × 23	120.1 ± 22.7	0.93607 ± 0.903	120	0.91833 ± 1.49	1.89	3.1 ± 7.6	0.93504 ± 0.900	0.109
25 × 25	120.6 ± 22.3	0.93584 ± 0.900	121	0.91827 ± 1.48	1.88	3.1 ± 7.5	0.93480 ± 0.897	0.111

[a]Mean ± CV.
[b]Other threshold prediction methods work better for these filters.

cluded those by Ramesh et al. (21), Otsu (14), Duda and Hart (3), and Gonzalez and Wintz (6).

A method based on the assumption that the filter separates the classes enough to create a minimum at the best threshold performed much better. One problem with the intermodal minimum, resulting from the large mixture distribution, was the presence of side peaks and noisy data in the histograms, as shown in Figure 4. The uncertainty created by this noisy appearance was improved by smoothing with a moving average and a moving polynomial fit. The polynomial fit was sped up by implementing it as a Savitzky-Golay FIR filter with the software provided by Press et al. (17). As also described by Press et al. (17), the moving average blunts peaks and valleys. As a result, it broadened the base of the large background peak and shifted the minimum to higher intensities.

The performance of the intermodal minimum was tested by application of all 120 filters to each of the 10 images. The 1200 10-bit histograms (with a range of −384 to 639) were formed and smoothed by 23-tap averaging and second order Savitzky-Golay filters. The intermodal minimum then found within an absolute search range of 115 from the location of the background peak. Limiting the search range eliminated the difficulty of locating the indistinct object peak. Dependence on the averaging filter was determined by testing the range of tap-lengths from 0 to 23. The intermodal minimum was found to increase by 1/4 the tap-length and this dependence was corrected.

The predictive performance of the intermodal minima is summarized in Table 3 by filter size as a comparison with the best thresholds. This data also includes the best possible fixed thresholds. The best thresholds achieve maximum segmentation accuracy and cannot be realized in practice because a priori knowledge of a standard is required. Instead, they provide a useful method for evaluating the success of threshold prediction.

The best threshold data in Table 3 demonstrate the

improvement obtained using the perceptron-trained filters. The mean classification ratios for filters larger than 3 × 3 improved to greater than 93% from 88% for the best threshold with no filter. Consistent with Figures 2 and 3 and Table 2, the sharpen filter reduced segmentation accuracy. The use of fixed thresholds resulted in about a 2% loss in segmentation accuracy over the best thresholds for filters larger than 3 × 3. Thus, the FIR segmentation accuracy was still much higher than the best threshold with no filter. The intermodal minimum as a predictor of the best threshold improved this to a loss of only about 0.11% for all filters larger than 3 × 3. This demonstrates the degree of threshold insensitivity obtained with the perceptron-trained filters. These filters improve segmentation accuracy even with fixed thresholds, but the improvement is greater with use of the relatively simple intermodal minimum for automatic thresholding.

Visualization of Segmentation Performance

Figure 5 displays the steps of image segmentation on Image 4. The sequence shows the original image, the filtered image, and the edge maps. The edge maps are a comparison of the manually segmented ideal, the identity at best threshold (threshold = 19, classification ratio 0.863) and a 15 × 15 perceptron-trained filter at the predicted threshold (threshold = 94, classification ratio 0.937). For both the identity and filtered results, a size threshold was applied to eliminate background noise and internal object holes were filled automatically as described. Select enlargements are also shown for detail. The filtered image exhibits the contrast enhancement of the filter along with some of the artifacts that arose in the process of creating the montage. Many of the line patterns in the background are due to moving and recopying the areas to fit them into the montage and were not present in the original microscopy images.
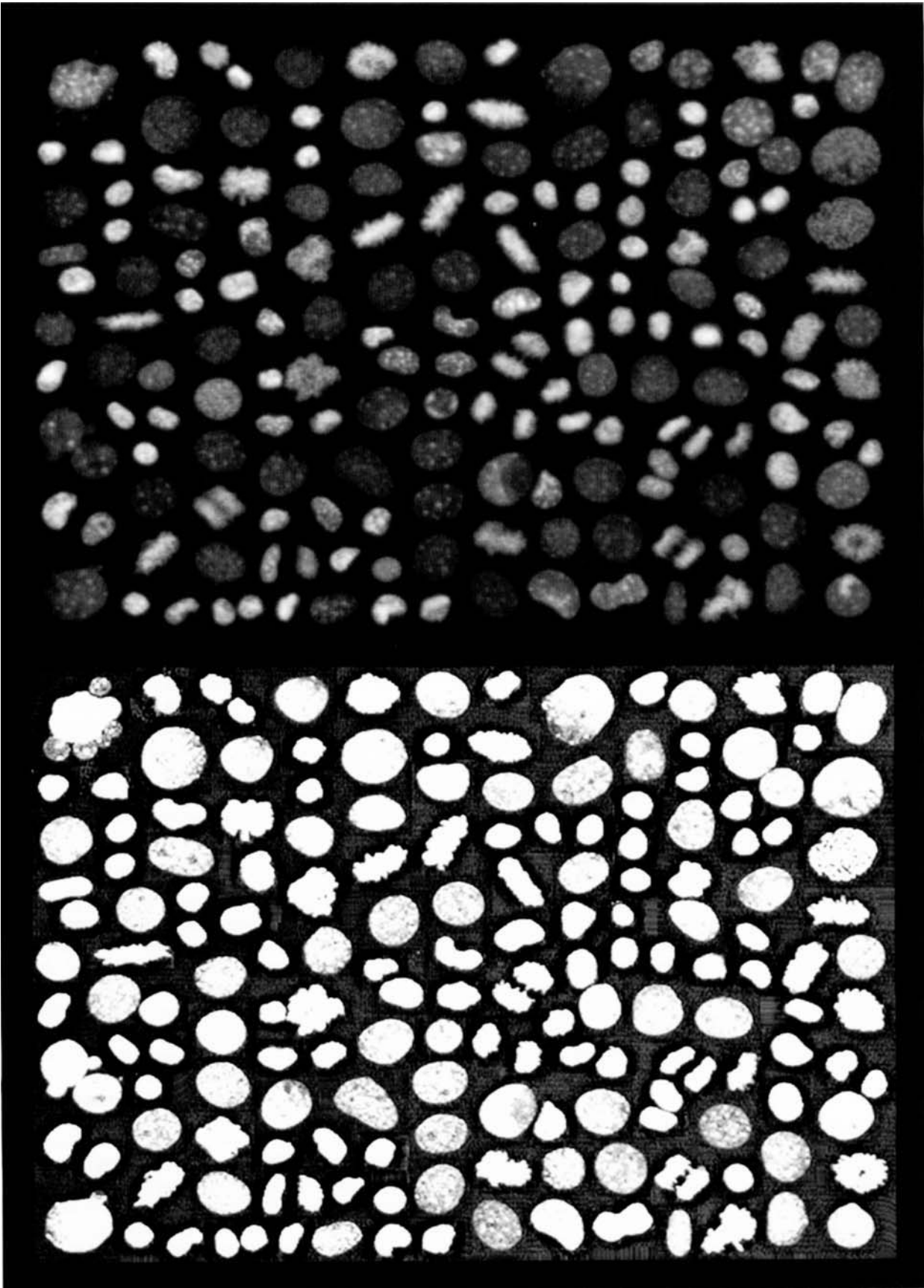
The differences in the edge maps in Figure 5 are most
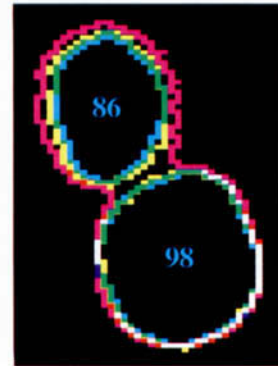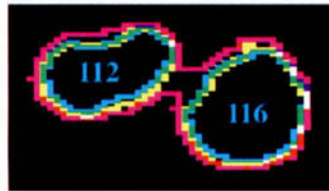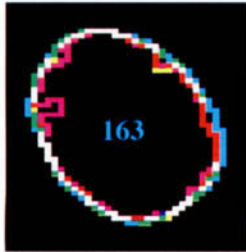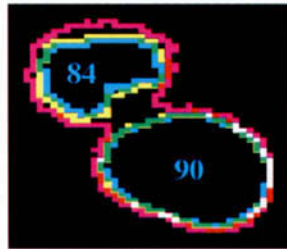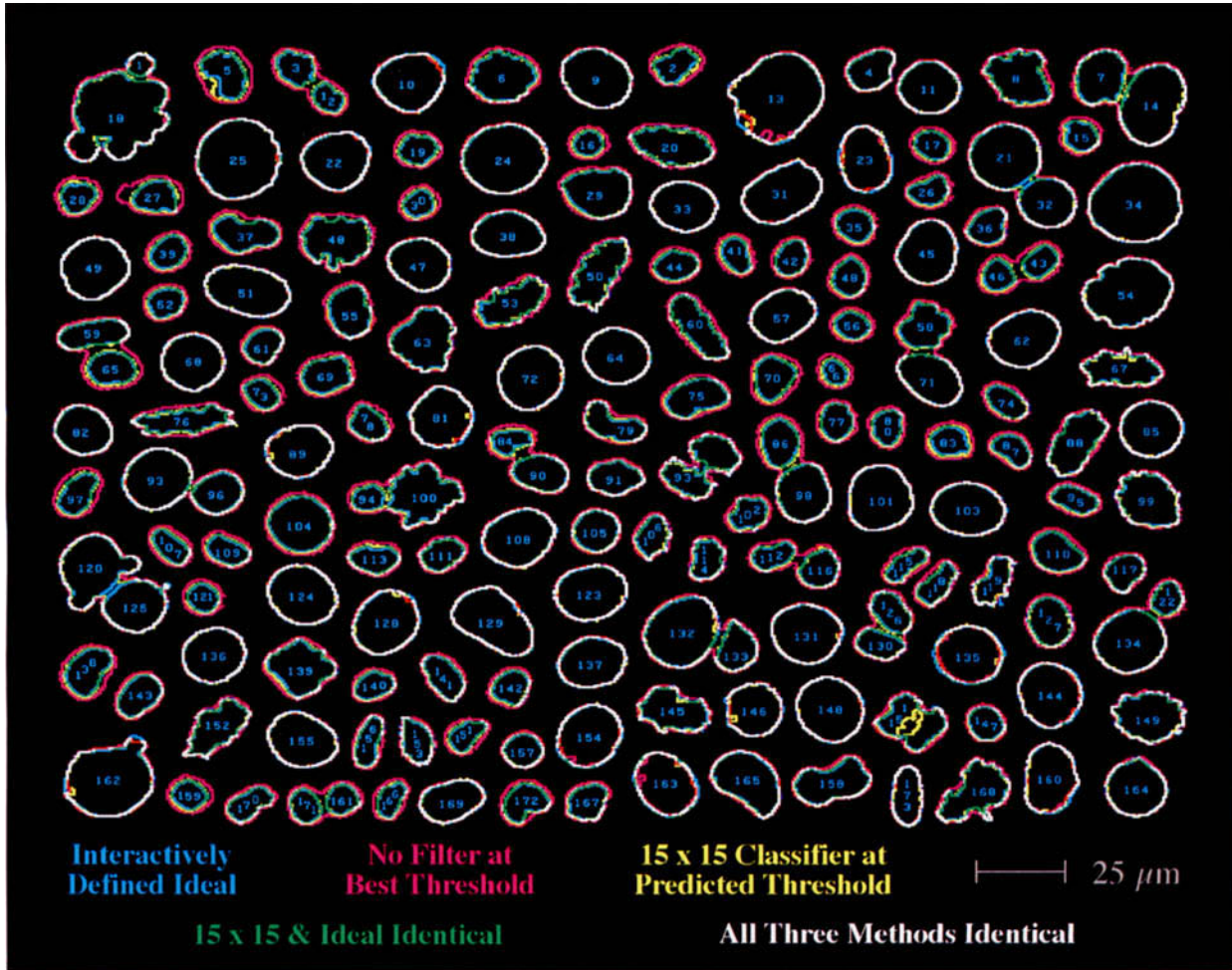
FIG. 5 (caption at right).

FIG. 5. Visualization of segmentation for Image 4 (Table 1). **Upper left panel:** The original image. **Lower left panel:** The result of a 15 × 15 classifier convolution (trained on Image 2). **The right panels:** The edge maps for the manually segmented ideal image (cyan), the applica-tion of best threshold with no filter (magenta), and the result of a 15 × 15 classifier filter at the predicted threshold of 94 (yellow). Enlarged views of selected objects are also shown.

Table 4
Trained vs. Untrained Classification Ratios

Training image	Test image[a]										Trained[b]	Mean untrained[c]	(%) trained - untrained
	1	2	3	4	5	6	7	8	9	10			
1	0.9384	0.9188	0.9385	0.9434	0.9391	0.9363	0.9458	0.9457	0.9440	0.9355	0.9384	0.9386	−0.0143
2	0.9322	0.9200	0.9372	0.9365	0.9310	0.9316	0.9414	0.9445	0.9405	0.9324	0.9200	0.9364	−1.7822
3	0.9224	0.9092	0.9308	0.9269	0.9137	0.9248	0.9357	0.9401	0.9362	0.9284	0.9308	0.9264	0.4773
4	0.9286	0.9142	0.9351	0.9366	0.9275	0.9306	0.9405	0.9443	0.9403	0.9324	0.9366	0.9326	0.4288
5	0.9315	0.9167	0.9361	0.9383	0.9346	0.9325	0.9424	0.9450	0.9415	0.9327	0.9346	0.9352	−0.0626
6	0.9343	0.9170	0.9357	0.9401	0.9343	0.9377	0.9458	0.9471	0.9437	0.9360	0.9377	0.9371	0.0582
7	0.9346	0.9162	0.9371	0.9418	0.9353	0.9371	0.9467	0.9473	0.9450	0.9364	0.9467	0.9367	1.0508
8	0.9310	0.9184	0.9351	0.9365	0.9298	0.9330	0.9422	0.9482	0.9408	0.9325	0.9482	0.9332	1.5733
9	0.9354	0.9195	0.9387	0.9430	0.9370	0.9367	0.9457	0.9485	0.9470	0.9356	0.9470	0.9378	0.9693
10	0.9323	0.9155	0.9378	0.9398	0.9315	0.9356	0.9450	0.9472	0.9446	0.9369	0.9369	0.9366	0.0324
Means	0.9321	0.9166	0.9362	0.9383	0.9314	0.9336	0.9431	0.9458	0.9423	0.9339	0.9377	0.9351	0.2731

[a]Means from 5 × 5 through 25 × 25 filters.
[b]Diagonal values copied.
[c]Means of the other 9.

obvious in the brightest and dimmest nuclear images. For the bright nuclei, segmentation of the unfiltered image at best threshold results in objects much larger than the ideal objects. This over-selection can be seen in most of the cell nuclei. In many cases the over-selection results in incorrectly segmenting two objects as a single object {1,18; 3,12; 7,14; 43,46; 59,65; 58,71; 84,90; 86, 98; 93,96; 94,100; 112,116; 126,130; 122,134; 132,133; 161,171}. In other cases where the borders are complicated (e.g., metaphase nuclei 50, 53, 76, and 168), the over-selection also smoothes the borders, removing potential useful shape information. For dim nuclei, on the other hand, no filter at best threshold sometimes results in too small an object size {13, 23, 144, 154, 160, 163}. The 15 × 15 perceptron-trained filter at the predicted threshold performs much better. This can be seen from the relative lack of yellow in the edge maps of Figure 5. Many of the yellow edges coincided with cyan (ideal) to create green, or blue and magenta (identity) to create white. In addition, most of the nuclei paired by segmenting the unfiltered image at best threshold were correctly recognized as two separate objects. The pair {120, 125} is an exception that may represent a case where the nuclei actually touch at this microscope resolution. Many of the problems with the dim nuclei are also corrected with application of the 15 × 15 perceptron-trained filter. There are practical limits to how dim an object can be before information is irretrievably lost. This may have occurred with the dimmest portion of nucleus 13. Although more of object 13 was correctly segmented by the perceptron-designed filter, the darkest portion is incorrectly segmented by both.

Figure 5 also shows that improvement in segmentation accuracy obtained using the best FIR filter for contrast enhancement decreases the number of incorrectly merged nuclei. Although no extra penalty was incorporated into the criterion function for merge errors, improving the pixel accuracy decreased the number of close proximity nuclei that were merged. A relatively small improvement at the edge can result in splitting

incorrectly merged objects. It may also be necessary to apply additional processing to detect overlapping objects, but it is important to recognize that accurate low-level segmentation does not merge adjacent nuclei that re not actually touching.

Trained vs. Untrained Performance

Supervised learning methods are only useful if the parameters fit using one set of data (trained) can be shown to work well against a new set of data (untrained). This is the reason for fitting the filters to each of the 10 montage images independently, rather than fitting to all 10 simultaneously. The 10 independent data sets and fits provide a practical way to explore the untrained error by comparison of each of the trained data sets with the other 9 images for which the filters were not trained.

The trained vs. untrained data is shown in Table 4. The first 10 columns display the average classification ratios for the 5 × 5 through 25 × 25 filters at best threshold for each pair. The diagonal values represent application of the filters to the image for which they were designed. The other 90 values convey the performance on new image for which the filters were not designed. All values are shown in to allow assessment of the uniformity. The final three columns summarize the performance. The first of these columns is the trained diagonal data copied for simpler comparison. The second is the mean of the nine untrained results in each row and the third is the percent difference of the trained and untrained. The last row displays the mean of each column. The classification ratio at best threshold is shown instead of at the predicted threshold to isolate the performance of the filter (for comparison, the mean of the percent Trained − Untrained for the predicted classification ratios was 0.3394).

The biggest difference between trained and untrained accuracy occurred with Image 2. The filters designed for Image 2 achieved higher accuracy on the images for they were not designed. This indicates that the source of increased error lies with the image, a conclusion further supported by the fact that this image showed the lowest

mean classification ratio for filters trained on all images. Image 5 resulted in the next lowest mean classification ratio and the filters trained on it also performed better on the untrained images. While this emphasizes the fact that some images are easier to segment than others, it also indicates that the amount of training data may be large enough that the accuracy is largely independent of the image used for training. Another way of determining the success of the training method is to compare the correlations of the trained data (diagonal) with the Training Image data (means of the rows) and the Test Image data (means of the columns). For Table 4, the linear correlation coefficients of 0.92 for the Test Image data and 0.45 for the Training Image data. Thus, the segmentation accuracy was more dependent on which image was tested than on which image was used for training, further supporting the conclusion that the amount of test data was adequate.

DISCUSSION AND CONCLUSIONS

Least squares designed spatial FIR filters for low-level segmentation of fluorescence-stained cell nuclei were shown to be capable of accurate, repeatable operation. Segmentation accuracy is important for image cytometry because of the likely utility of morphometry envisioned from images. It can be argued that errors in segmentation occurring in the blurry region at the edges of an object where the intensities are low may not produce significant errors in the integrated intensity measurements that result, for example, in DNA content. But these errors are expected to be extremely critical for measurements such as area and perimeter that would be useful in diagnostic pathology or basic research. With the flow cytometer on the other hand, where the locations of the beginning and end of a fluorescence stained object in the one-dimensional intensity data stream produced by the photomultiplier tube are used primarily for integrated intensity and detailed morphometry is not possible, this accuracy is not as critical.

The goals did not include separation of overlapping objects, but this segmentation process did show a decrease in errors produced by incorrect merging of adjacent, nonoverlapping objects (see Fig. 5). Erroneously split or merged objects would create disproportionately large errors in all subsequent object-specific measurements. One might be tempted to include penalties for incorrectly split or merged nuclei in the error criterion in an attempt to reduce errors further. The case of incorrectly split nuclei, however, did not arise in any of the 1,070 objects in this training set, in spite of the purposeful addition of very dim nuclei. Thus, this method did not appear to be predisposed to the introduction of incorrect splits. Specific error-weighting of erroneously merged objects should be approached with caution. Merge errors are an artifact of either the limits of microscope resolution (with adjacent objects), or the projection of a three-dimensional specimen into a two-dimensional image (with overlapping objects). For the purpose of finding the DNA content, area, perimeter or most any other mea-

surement except object count, the projection creates an artifact for which information is irretrievably lost and which would be appropriately addressed or compensated for at some higher-level processing stage, perhaps by employing domain specific knowledge. Thus, it makes sense to consider the FIR filter and threshold steps as low-level segmentation and follow with a refining recognition step based on shape or other criteria to identify overlapping objects. Further processing could be applied (e.g., the watershed algorithm on the small image area containing the merged nuclei) to obtain a better estimate of the object count, and a flag used for elimination of overlapping objects from integrated intensity and spatial data. Using the measured data rather than the larger images, it should be possible to perform this and other subsequent classification steps more rapidly. This strategy allows the real-time FIR filter to perform the task for which it is most capable, while limiting the number and complexity of the global image operations that require dedicated image processing hardware.

The quality of automatic classification of the cell cycle phase or even the cell type from measurements like perimeter and area will be dependent on the underlying segmentation accuracy. In Figure 5, one could easily imagine using a combination of measurements including the perimeter or a measure of its spatial frequency to classify metaphase cell nuclei (e.g., 53, 57, and 67). The complicated perimeters of these nuclei would be grossly underestimated by an over-selection as small as only 1 or 2 pixels filling edge indentations. Such an error would make metaphase classification more difficult. The physical existence of sharp points on the edges of these nuclei is also the reason that using binary morphology after thresholding to "clean up" possibly noisy edges should be approached with caution. Such a step would be warranted only if the edge noise occurred at a greater resolution than the physical edge features (e.g., the chromosome arms).

Achieving accurate segmentation with FIR filters borrows from the idea of using deconvolution to sharpen an image. Deconvolution has been used by Agard et al. (1) and many others for removal of out-of-focus information in three-dimensional fluorescence microscopy. This work has shown that practical deconvolution is considerably more complicated than the single application of an FIR filter. In this context, the segmentation method used here can be thought of as incorporating the power of the best single-step deconvolution. Freeing the filter from the constraint of producing a "sharp" version of what the image should really look like without the blur, and asking only that it create contrast in order to locate the edge, is key in achieving high accuracy with this linear approximation. While it might be possible to use deconvolution to achieve a similar result, the best deconvolution techniques are iterative and extremely computationally intensive and are not likely to be cost-effectively implemented in real time for many years.

The use of an FIR classifier for segmentation should be applicable to any image where the primary task is sharp-

ening and contrast enhancement. Although this is simplest for images consisting of two basic pixel classes, it is in principle extensible to images containing multiple pixel classes (e.g., by sequential application of the two-category classifier). If real-time operation is not required and the differences between object classes consist of more complicated patterns, the neighborhood operator can be made nonlinear to incorporate a more elaborate model of the pattern. Differences in contrast (or intensity S.D.), for example, can be described by a second order neighborhood operator. Whereas the FIR filter cannot create contrast between regions of equal mean and different S.D. the second-order neighborhood operator can. The perceptron criterion could also be applied for design of nonlinear neighborhood operators. Although nonlinear operators would be more computationally intensive, the segmentation step would still be noniterative and real-time hardware implementation more easily achieved than with iterative techniques designed for the same more complicated textures and patterns.

The accurate, real-time segmentation achieved here is an important step in the development of an image cytometry instrument capable of the same operator-independent level of automation currently available with flow cytometers. The choice of the perceptron criterion as the error function for FIR filter design helped create the necessary contrast to simplify automated threshold selection and nearly eliminate the errors associated with it. Automated spatial FIR filter design resulted in the best linear approximation of deconvolution for segmentation, as well as the best linear approximation of trained-technician segmentation. These manually segmented standard images are laborious and subjective, and future work may identify an automated method that is more objective and accurate than manual segmentation, but slower and more complex than an FIR filter. Thus it is also noted that the technique described here produces a best linear approximation given any standard image, regardless of the method used in its creation. Because accuracy requirements may often be underestimated, and there are important subtleties in measuring segmentation performance in the context of biomedical images, they have been considered in terms of the reliability of subsequent processing expected to utilize the segmented data as input. Further development of measures of segmentation accuracy on morphometry performance in cell classification and other applications is warranted. With the additional advantage of accurate morphometry, a device employing these segmentation methods may eventually have an even more dramatic impact on basic biomedical research and on clinical applications than the flow cytometer.

ACKNOWLEDGMENTS

LITERATURE CITED

1. Agard DA, Hiraoka Y, Shaw P, Sedat JW: Fluorescence microscopy in three dimensions. In: Fluorescence Microscopy of Living Cells in Culture, Part B, Methods in Cell Biology, vol. 30, Wang YL, Taylor DL (eds). Academic Press, San Diego, 1989.
2. Dom B, Blanz WE, Cox C, Steele D, Dorundo A: The segmentation engine: a real-time image segmentation subsystem. Machine Vision and Applications in Industrial Inspection II, San Jose, SPIE Proceedings 2183:1–16, 1994.
3. Duda RO, Hart PE: Pattern Classification and Scene Analysis. John Wiley & Sons, New York, 1973.
4. Embree PM, Kimble B: C Language Algorithms for Digital Signal Processing. Prentice Hall, Englewood Cliffs, 1991.
5. Fu KS, Mui JK: A survey on image segmentation. Pattern Recognition 13:3–16, 1981.
6. Gonzalez RC, Wintz P: Digital Image Processing, 2nd ed. Addison-Wesley, Menlo Park, 1987.
7. Hamada S, Fujita S: DAPI staining improved for quantitative cytofluorometry. Histochemistry 79:219–226, 1983.
8. Hunter EA, Price JH, Gough DA: Applications of optimal filters to segmentation of microscope images. Proceedings of the 15th Annual International Conference of the IEEE Engineering in Medicine and Biology Society, San Diego pp 487–488, 1993.
9. Jain AK: Fundamentals of Digital Image Processing. Prentice Hall, Englewood Cliffs, 1989.
10. Levine MD, Nazif AM: An experimental rule-based system for testing low level segmentation strategies. In: Multicomputers and Image Processing, Preston K, Uhr L (eds). Academic Press, New York, 149–160, 1982.
11. Levine MD, Nazif AM: Dynamic measurement of computer generated image segmentations. IEEE Transactions on Pattern Analysis and Machine Intelligence 7:155–164, 1985.
12. Lim YW, Lee SU: On the color image segmentation algorithm based on the thresholding and the fuzzy c-means techniques. Pattern Recognition 23:935–952, 1990.
13. Lockett SJ, Jacobson K, O'Rand M, Kaufman DG, Corcoran M, Simonsen MG, Taylor H, Herman B: Automated image-based cytometry with fluorescence-stained specimens. Biotechniques 10:514–519, 1991.
14. Otsu N: A threshold selection method from gray-level histograms. IEEE Transactions on Systems, Man, and Cybernetics 9:62–66, 1979.
15. Pal NR, Pal SK: A review on image segmentation techniques. Pattern Recognition 26:1277–1294, 1993.
16. Pal NR, Bhandari D: Image thresholding: some new techniques. Signal Processing 33:139–158, 1993.
17. Press WH, Teukolsky SA, Vetterling WT, Flannery BP: Numerical Recipes in C, 2nd ed. Cambridge University Press, Cambridge, 1992.
18. Price JH: Scanning Cytometry for Cell Monolayers. Ph.D. Dissertation, Applied Mechanics and Engineering Sciences, Bioengineering, University of California, San Diego, 1990.
19. Price JH, Gough DA: Nuclear recognition in images of fluorescent stained cell monolayers. SPIE, Applications of Digital Image Processing XIII, 1349:294–300, 1990.
20. Price JH, Gough DA: Comparison of phase-contrast and fluorescence digital autofocus for scanning microscopy. Cytometry 16:283–297, 1994.
21. Ramesh N, Yoo J-H, Sethi IK: Thresholding based on histogram approximation. IEE Proceedings, Vision, Image and Signal Processing 142:271–279, 1995.
22. Russ JC: Computer-Assisted Microscopy. Plenum, New York, 1990.
23. Russ JC: The Image Processing Handbook. CRC, Ann Arbor, 1992.